Electrochimica Acta 525 (2025) 146088

Contents lists available at ScienceDirect

Electrochimica Acta

journal homepage: www.journals.elsevier.com/electrochimica-acta

Mg- and Ni-modified Fe_2O_3@rGO as enhanced peroxide scavenger cocatalysts in oxygen reduction reaction

Leonardo Balducci [a,*], Mohsin Muhyuddin [b], Hamideh Darjazi [c,d,**], Giuseppina Meligrana [c,d], Carlo Santoro [b], Francesco Nobili [a,d]

[a] School of Science and Technology - Chemistry Division, University of Camerino, Via Madonna delle Carceri, ChIP, 62032, Camerino, Italy
[b] Electrocatalysis and Bioelectrocatalysis Laboratory, Department of Materials Science, University of Milano-Bicocca, U5, Via Cozzi 55, 20125, Milano, Italy
[c] Group for Applied Materials and Electrochemistry - GAME Lab, Department of Applied Science and Technology - DISAT, Politecnico di Torino, Torino, 10129, Italy
[d] GISEL—Centro di Riferimento Nazionale per i Sistemi di Accumulo Elettrochimico di Energia, INSTM, via G. Giusti 9, 50121, Firenze, Italy

ARTICLE INFO

Keywords:
Modification effect
Fe_2O_3
Reduced graphene oxide
Electrocatalysts
Semiconductor
Oxygen reduction reaction

ABSTRACT

The exploitation of graphene oxide (GO)-based composites for fuel cell electrocatalysts has gained significant interest, yet the integration of iron oxide nanoparticles grafted onto GO, doped with different metals, remains relatively unexplored. This study aims to fill this gap by synthesizing and characterizing Fe_2O_3 nanoparticles grafted on GO doped with two different metals, specifically magnesium and nickel, each at three different concentrations (6%, 12%, and 18% by weight). The successful doping and incorporation of Fe_2O_3 on the GO matrix is confirmed using X-ray diffraction (XRD) and Raman spectroscopy. Scanning electron microscopy (SEM) provides insights into the morphology and dispersion of Fe_2O_3 nanoparticles on the GO surface. Rotating Ring Disk Electrode (RRDE) is used to analyze the electrochemical activities toward the oxygen reduction reaction (ORR). The results demonstrated improved electrocatalytic activity and selectivity with increasing metal concentration. Notably, the electrocatalysts with 6% Mg and 6% Ni doping exhibit superior peroxide scavenging properties. When 6% Ni is mixed with FePc600, it provides additional active sites devoted to the peroxide scavenging increasing the limiting current from 4.69 to 5.62 mA cm^{-2}, halving the peroxide production, passing from 5.1% to 2.9%. Overall, this study provides insights into the tunable properties of Fe_2O_3@GO composites through metal doping, offering a versatile approach to enhance the performance of composite materials in various technological applications, and specifically suggests that Fe_2O_3 grafted on GO, modified with Mg and Ni, holds significant potential as a cocatalyst for ORR in energy devices such as alkaline fuel cells.

1. Introduction

Fuel cells (FCs) are recognized as one of the most promising electrochemical technologies for energy production applications [1]. Among the various electrocatalysts for FCs, Pt-based electrocatalysts have been considered the benchmark for low-temperature FC applications due to their high electrocatalytic activity toward oxygen reduction reaction (ORR) [2]. However, the high cost and limited availability of platinum have been the major hurdles in the widespread commercialization of FC devices. Therefore, finding efficient and cost-effective alternatives to Pt-based electrocatalysts for ORR has become a key area of investigation in the field of FCs [3–5], and extensive research efforts have been focused on the development of Pt-free electrocatalysts with enhanced stability and durability for ORR.

The cathodic ORR can occur in three different main pathways: (i) 2 e^- partial reduction with H_2O_2 / HO_2^{ads} intermediate production; (ii) 4 e^- total reduction in which O_2 is converted and H_2O/OH^- and (iii) with a 2 + 2 e^- reaction mechanism that involves step (i) with H_2O_2 / H_2O^- intermediate production that is further reduced to H_2O/OH^- on the same or on a different active site [6,7]. Two electron pathway is the preferred route for hydrogen peroxide electrosynthesis, while direct 4 e^- transfer is the desired and pursued pathway for the energy conversion in fuel cells.

In an acidic electrolyte, the four-electron pathway (Eq. (1)), the two-electron pathway (Eq. (2)) and the 2+2 electron pathway (Eq. (3))

* Corresponding author.
** Corresponding author at: Group for Applied Materials and Electrochemistry - GAME Lab, Department of Applied Science and Technology - DISAT, Politecnico di Torino, Torino, 10129, Italy.
E-mail addresses: leonardo.balducci@unicam.it (L. Balducci), hamideh.darjazi@polito.it (H. Darjazi).

https://doi.org/10.1016/j.electacta.2025.146088
Received 23 December 2024; Received in revised form 18 March 2025; Accepted 19 March 2025
Available online 20 March 2025

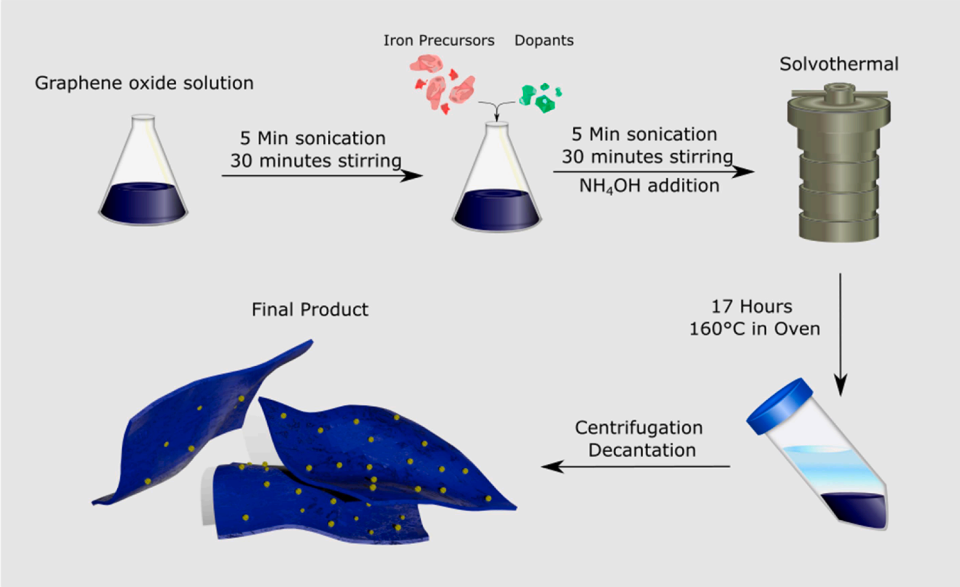

Fig. 1. Schematic illustration of the Synthetic Methodology; where final products are pristine- and doped-Iron Oxide.

mechanisms are reported to be:

$$O_2 + 4H^+ + 4e^- \rightleftharpoons 2H_2O \quad (1)$$

$$O_2 + 2H^+ + 2e^- \rightleftharpoons H_2O_2 \quad (2)$$

$$H_2O_2 + 2H^+ + 2e^- \rightleftharpoons 2H_2O \quad (3)$$

When energy conversion in alkaline media, with the final production of hydroxide anions, is desired, the favorable mechanism is the $4e^-$ pathways (Eq. (5)) as expressed by the following equation:

$$O_2 + 2H_2O + 4e^- \rightleftharpoons 4HO^- \quad (5)$$

While the 2+2 electron can be expressed as follows (Eqs. (6) and (7)):

$$O_2 + * + \ H_2O + 2e^- \rightleftharpoons HOO^- * + HO^- \quad (6)$$

$$HOO^- + H_2O + 2e^- \rightleftharpoons 3HO^- \quad (7)$$

Regarding the formation of water the existence of an overpotential up to 400 mV is the main limiting factor an ORR electrocatalyst has to face [6].

In general, the FCs electrocatalyst may be divided into three main groups: (I) Platinum group metal (PGM-based) materials, (II) Carbonaceous metal-free materials, and (III) Platinum metal group-free (PGM-free) materials [8,9]. The use of carbonaceous materials has significantly raised attention thanks to their common properties such as high surface area, electrical conductivity, corrosion resistance, and mechanical and thermal stability; moreover, they rely on an industrial production optimization that allows them to be greatly available. Despite this, FC cathodes purely composed of carbonaceous materials show high overpotential and low reaction kinetics which limit their application. Moreover, it is well known that carbonaceous materials that do not contain transition metals, whether dispersed or in form of nanoparticles, undergo an ORR through 2 e^- transfer mechanism, which is undesirable for FCs application.

To overcome the problems mentioned above, PGM-free carbonaceous composite materials containing transition metals have been extensively studied for their ability to decrease the overpotential and consequently increase the overall activity [8,10,11]. Among these PGM-free electrocatalysts, those iron-based ones stand out since Fe is the most abundant and cost-effective transition metal on Earth. Numerous studies have demonstrated that Fe-based electrocatalysts can serve as a viable alternative to Pt-based materials, displaying comparable activities during ORR, especially in neutral and alkaline media. Among the different electrocatalytic systems, Fe_2O_3 demonstrates noteworthy potential to performe as an electrocatalyst for FC applications, such as mechanical, thermal stability, and wettability to water [12,13]. There are two crystal forms of α-Fe_2O_3 (hematite) and γ-Fe_2O_3 (maghemite) in nature [14]. In addition, these oxides can be synthesized in several ways and for different applications, most of them requiring low-temperature treatment and starting from low-cost precursors, thus making them well-suited for industrial large-scale production [12,15]. However, despite their good efficiency and low production cost, the commercialization of these electrocatalysts has been hindered by their lack of selectivity in the ORR pathways and their sluggish reaction kinetics. Ongoing research aims to enhance the selectivity of these catalysts to overcome these challenges and expand their use in fuel cell technology [16,17]. Notably, studies have demonstrated that α-Fe_2O_3 exhibits superior ORR electrocatalytic activity, as evidenced by its lower onset and peak potential compared to γ-Fe_2O_3. Furthermore, α-Fe_2O_3 promotes a more efficient four-electron-dominant ORR process, highlighting its enhanced catalytic performance and greater potential for widespread application [18].

In this study, we examine how varying levels of Mg and Ni in the material affect Fe_2O_3-based electrocatalysts, focusing on their structural and electrochemical characteristics. This approach aims to clarify how Ni and Mg modifiers concentrations influence structure, morphology, and peroxide scavenging properties, helping establish a link between the type and amount of the two modifiers and electrocatalyst performance. To synthesize these materials, a one-pot solvothermal technique has been utilized since it offers reproducibility, scalability, and high yield [15,19]. The structural features have been investigated to confirm the presence of Ni and Mg and their effect on crystal lattice and morphology. The electrocatalytic performance are analyzed by voltammetry at Rotating Ring Disk Electrodes (RRDE) to assess the enhanced activity of the developed materials.

2. Experimental

2.1. Catalysts synthesis

All the chemicals have been purchased from Merck and used without any further purification. The synthesis has been carried out following a method previously reported in literature [15]. In detail, 30 mg of

Graphene Oxide (GO) in 30 ml of water was ultrasonicated for 10 min. Subsequently, 31.09 mg of $(NH_4)_2Fe(SO_4)_2$ have been added to the suspension and ultrasonicated for a further 10 min. Finally, 30 μl of NH_4OH have been added and ultrasonicated for 2 h at room temperature. The final dispersion was transferred to a 70 ml autoclave reactor and heated at 150 °C for 15 h in an oven. To obtain the final product the suspension was centrifuged and the supernatant solution was removed, the collected powder then was redispersed in distilled water and centrifuged. This procedure was repeated two more times, to ensure the complete removal of the base, and then the collected wet powder was dried at 60 °C overnight. The same procedure was applied for the synthesis of the modified catalysts with the addition of different amounts of $Mg(NO_3)_2$ and $Ni(NO_3)_2$ at 6%, 12%, 18% Mg/Fe or Ni/Fe mass ratios, respectively, and the addition of a slight excess of the base was added (3/6/9 μl, respectively). All the catalysts will be referred to in the following text according to their concentration of modifiers such as Mg6%, Mg12%, Mg18%, Ni6%, Ni12% and Ni18% (see Fig. 1**.** In the following manuscript, the electrocatalysts will be referred to either by their full nomenclature (e.g., $M_{X\%}Fe_2O_3$@rGO) or by a shortened form (e.g., $M_{X\%}$) for conciseness.

2.2. Physico-chemical characterization

X-ray diffraction (XRD) and Raman spectroscopy were used for the determination of the structures and phases present in the samples. Crystalline phases were identified through X-ray diffraction analysis (XRD) using a Panalytical Xpert3 MRD system. The analysis was conducted at room temperature with Cu Kα radiation, operating at a voltage of 40 kV and a current of 40 mA, over a 15–70° 2θ range. Raman spectroscopy was performed with a Horiba IHR 320 (excitation wavelength 532 nm) from 100 to 3500 cm^{-1}. Rietveld refinement of the XRD patterns was performed using the FullProf software. To correctly quantify the iron content and the Iron to C ratio thermogravimetric analysis has been carried out by a Perkin Elmer STA 6000. The investigation of the morphological features was carried out with a FE-SEM Cambridge Stereoscan 360 electron microscope operating at 5 kV coupled with an energy-dispersive X-ray spectrometer (EDX).

X-ray photoelectron spectroscopy (XPS) analyses were performed using a PHI 5000 Versa Probe instrument from ULVAC-PHI (Physical Electronics Inc., Kanagawa, Japan). The instrument employed monochromatic Al Kα radiation with an energy of 1486.6 eV as the X-ray source. Two different pass energy settings were used: 187.75 eV for the survey spectra and 23.5 eV for the high-resolution (HR) spectra. During the measurements, charge compensation was maintained using a combination of an electron beam and a low-energy Ar beam system.

2.3. Ink preparation

The ink was prepared by a standardized procedure applied to each sample. In detail, the samples were mixed with KJB in a 20:80 electrocatalyst-to-KJB ratio and ground for 20 min to ensure homogenization. Afterward, 5 mg of catalyst was dispersed in 985 μl of isopropanol and ultrasonicated for 3 min. Consequently, 15 μl of Nafion was added to the solution and the ink was sonicated for another 20 min. Finally, 28.5 μl of the ink was deposited on the surface of the working electrodes with a final (doped)Fe_2O_3@rGO overall loading of 0.6 mg/cm^2.

To assess the effective peroxide scavenging properties, a composite material with Iron-Phthalocyanine (FePc600) was created with 2 different ratios $M_xFe_2O_3$@rGO/FePc600, 20:80 and 80:20. The synthesis of FePc600 was previously described [20]. These inks have been prepared with the same standardized procedure previously discussed [20].

2.4. Electrochemical characterization

The electrochemical activity of the synthesized species by Rotating Ring Disk Electrodes (RRDE) with a Pine Research (Durham, NC) cell setup. The electrocatalysts were coated on the surface of a rotating-disk glassy carbon working electrode, which was assembled with a Pt ring electrode, Pt wire was used as a counter electrode, and Ag/AgCl (3M KCl, $E = 0.197$ V vs. RHE). The electrodes were immersed in an O_2-saturated 0.1 M KOH solution.

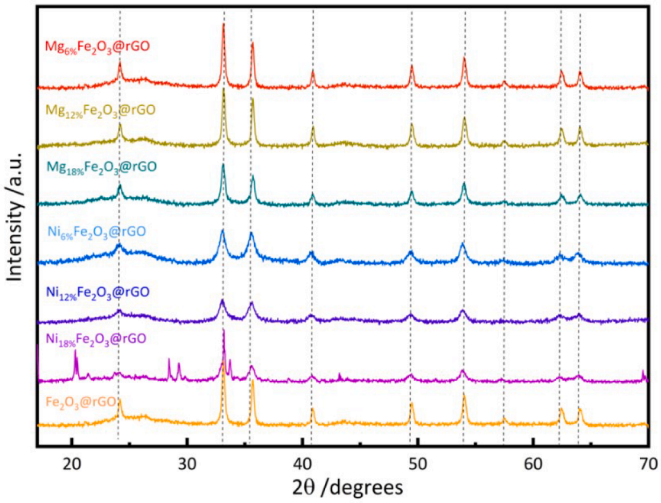

Fig. 2. XRD patterns of all samples.

The characterization was conducted using a CHI832 bipotentiostat (CH Instruments, Austin TX) coupled with a Pine model 636 Rotator with a maximum rotating speed of 1600rpm. To investigate the performance of the electrocatalyst, Linear Sweep Voltammetry (LSV) was performed. This was carried out from 0.150 V to −1.05 V vs Ag/AgCl, setting the ring potential at 0.150 V and at a scan rate of 5 mVs^{-1}. All the scans were performed at 1600 rpm and at room temperature. All voltages are reported vs. Reference Hydrogen Electrode (RHE) potential.

3. Results and discussion

3.1. Structural and morphological characterizations

The structural phase and crystallinity were investigated by XRD. Fig. 2 shows the diffraction peaks for all the samples. The diffraction patterns of Fe_2O_3@rGO, $Mg_{6\%}Fe_2O_3$@rGO, $Mg_{12\%}Fe_2O_3$@rGO, $Mg_{18\%}Fe_2O_3$@rGO, $Ni_{6\%}Fe_2O_3$@rGO, and $Ni_{12\%}Fe_2O_3$@rGO show common diffraction peaks, namely (012), (104), (110), (113), (024), (116), (018), (214), and (300) which are representative of rhombohedral α-Fe_2O_3 (hematite) phase with space group R-3c [21,22]. The lack of (001) peak of GO at 11.01° and the presence of (002) broad feature at 26.8°, typical of rGO, reveal that the oxygen-containing groups have been removed, suggesting that most of GO has been reduced to rGO upon hydrothermal synthesis [15,19,23]. The reduction of GO to rGO is beneficial in terms of electron conductivity. The diffraction patterns show no evidence of additional phase formation after doping, this suggests that the modification takes place mainly or totally in the internal structure of the α-Fe_2O_3. The diffraction pattern of $Ni_{18\%}$ Fe_2O_3@rGO reveals, as a main feature, the presence of an additional maghemite γ-Fe_2O_3 phase, with a space group of $P4_32_12$. This is evidenced by the presence of distinct sharp peaks at 33°, along with smaller peaks around 30°, 43°, and 70°, which in some cases overlap with the diffraction patterns of hematite [24]. In addition, a few extra peaks can be observed, which are related to the presence of $Ni(OH)_2$ [25].

To ensure accurate structural identification, Rietveld Refinement of the XRD patterns was conducted using the profile matching method within the FullProf Suite software. The results, shown in **Fig. S1** and summarized in **Table S1**, consistently indicate that all samples except

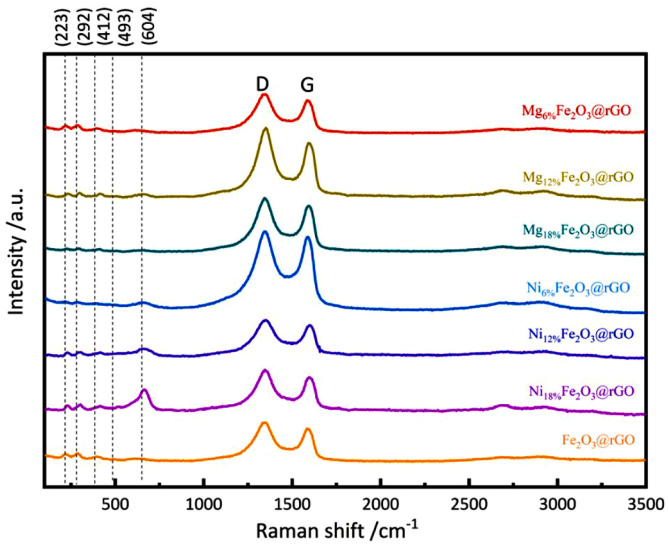

Fig. 3. Raman spectra for all samples.

$Ni_{18\%}Fe_2O_3$@rGO maintain a rhombohedral hexagonal structure, albeit with slight variations in lattice parameters. Notably, the doped samples exhibit slightly smaller lattice parameters and reduced cell volumes compared to the pristine sample. In particular, the $Ni_{6\%}Fe_2O_3$@rGO sample demonstrates the most significant reduction, with a cell volume of 302.1 Å^3 compared to 304.70 Å^3 for the pristine sample.

This reduction in lattice parameters could tentatively be attributed to: i) rhombohedral lattice distortion to accommodate the Ni and Mg modifiers, ii) the charge variation in the oxide structures induced by doping, potentially leading to the formation of oxygen vacancies aimed at restoring charge neutrality. The resulting smaller unit cells, coupled with the presence of oxygen vacancies, may prove advantageous for electron transfer kinetics, electron conduction within grain boundaries [26], molecular oxygen conductivity [27], and, consequently, better electrocatalytic activity. In light of these considerations, it can be expected that the $Ni_{6\%}Fe_2O_3$@rGO catalyst may possess the best performance among all the catalysts synthesized. It is reported in literature [28,29] that the formation of additional phases (as, in this case, the additional maghemite γ-Fe_2O_3 evidenced in the $Ni_{18\%}$-doped Fe_2O_3 diffraction profile) may be due to excessive amounts of modifiers or particular synthesis conditions, and may potentially lead to limitations in the efficiency of doped oxide grafting to the GO substrate and, as a consequence, to hindered catalytic activity [30]. The average hematite crystallite size (D) was estimated using the Debye-Scherrer equation as follows:

$$D = \frac{K\lambda}{\beta \cos\theta} \tag{8}$$

where $k = 0.9$ is the shape factor, $\lambda = 0.15418$ nm corresponds to the CuKα wavelength, θ is the Bragg diffraction angle and β represents the FWHM in Radians [31]. The d_{hkl}-spacing, lattice parameters, and unit cell volume of the obtained electrocatalysts were determined through XRD data analysis, Bragg's law, and Rietveld refinement based on powder diffraction data. Crystallite size estimations were performed using the two most intense peaks at approximately 33° and 35°, with the results summarized in Table S1. The calculated crystallite sizes range between 15.5 and 50.9 nm, with $Ni_{6\%}Fe_2O_3$@rGO and $Mg_{6\%}Fe_2O_3$@rGO exhibiting the smallest crystallite sizes.

The Raman spectra offer valuable information on the reduction of GO to rGO and the extent of nanocomposite formation, shown in Fig. 3. Notably, the spectra reveal two significant bands: the D band at 1358 cm^{-1}, indicating structural defects (A_{1g} mode), and the G band at 1597 cm^{-1}, corresponding to sp [2] carbon domains (E_g mode). In addition to the D and G bands, Fe_2O_3 peaks can be identified by comparison with pure α-Fe_2O_3 (hematite) Raman spectra, reported in **Fig. S2**. These peaks are associated with two classes of Raman active vibration modes: the symmetric stretching of Fe-O bond A_{1g} vibration modes at 223 and 493 cm^{-1}, and the symmetric and asymmetric bending of Fe-O bond Eg modes at 292, 412, and 604 cm^{-1} [32–34]. The additional peak in $Ni_{18\%}Fe_2O_3$@rGO at ≈ 720 cm^{-1} can be ascribed to the γ-Fe_2O_3 phase already evidenced in the XRD analysis [30,35].

Scanning Electron Microscopy (SEM) was carried out for all samples and the corresponding micrographs are shown in Fig. 4. All the electrocatalysts show similar nanoparticle dimensions in the range of 30 nm to 75 nm compared to the pristine iron oxide shown in **Fig. S3**. The nanoparticles are well distributed on the graphene oxide with a low degree of agglomeration. The nano-sized particles and their distribution are fundamental for the electrocatalytic activity, displaying a high

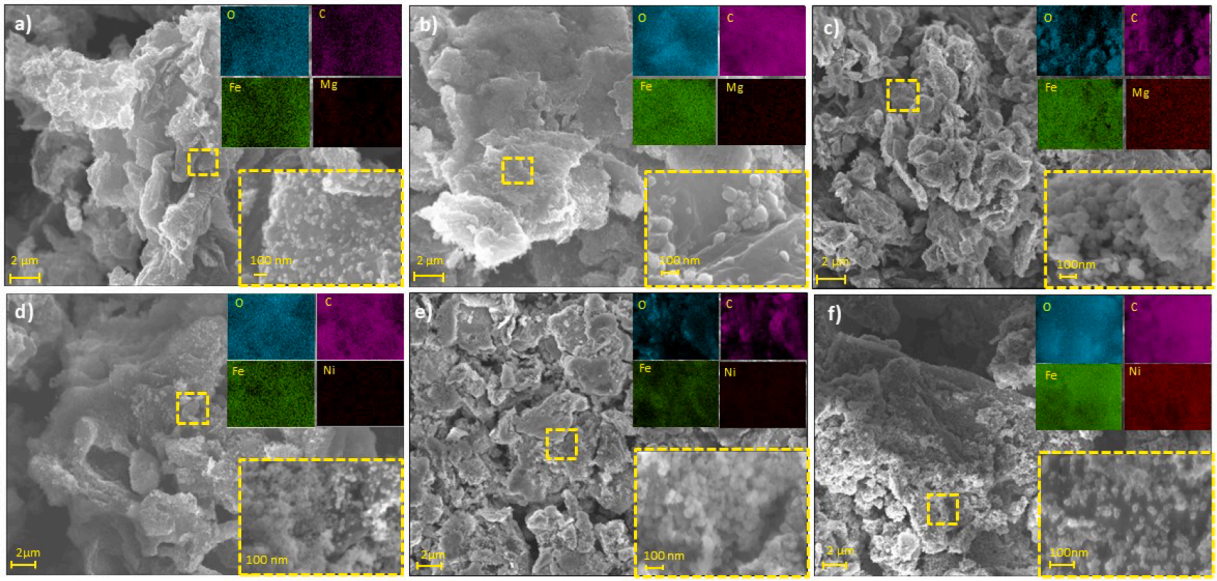

Fig. 4. SEM and Mapping comparison between $Mg_{6\%}Fe_2O_3$@rGO (a), $Mg_{12\%}Fe_2O_3$@rGO (b) and $Mg_{18\%}Fe_2O_3$@rGO (c), $Ni_{6\%}Fe_2O_3$@rGO (d), $Ni_{12\%}Fe_2O_3$@rGO (e) and $Ni_{18\%}Fe_2O_3$@rGO (f).

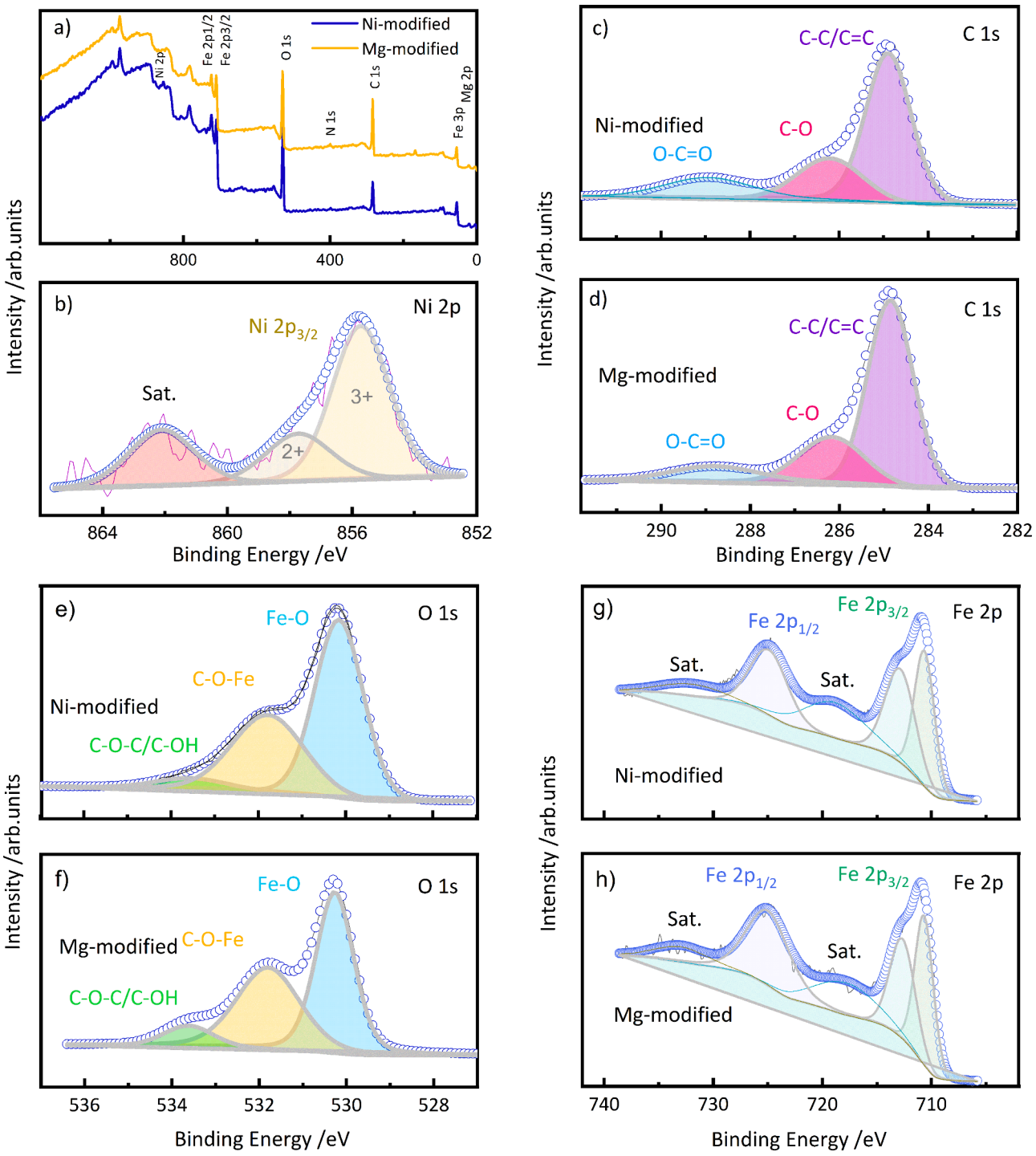

Fig. 5. XPS analysis on $Ni_{6\ \%}Fe_2O_3$@rGO and $Mg_{6\ \%}Fe_2O_3$@rGO.

surface volume ratio which is beneficial in terms of Turn Over Number (TON) and/or Turn Over Frequencies (TOF). The smallest particle sizes were observed in the $Mg_{6\%}$ and $Ni_{6\%}$. The EDX mapping shows a homogeneous distribution of the elements for all the catalysts, and the corresponding elemental analysis confirms that the concentration of the modifiers is around the expected values with negligible variations (**Table S2**).

To evaluate the carbon content and the electrocatalyst-to-carbon ratio, thermogravimetric analysis was performed in **Fig. S4**. All the materials show comparable (doped)Fe_2O_3/C ratios ranging from 36 % to 39 %, in agreement with the reference values reported in literature [15]. Based on the electrode preparation procedure, this corresponds to an approximate (doped)Fe_2O_3 loading of 78–65 μgcm^{-2}.

To elucidate the role of doping and the chemical states of the electrocatalysts, XPS has been carried out. Fig. 5 shows the result of the XPS analysis performed on $Mg_{6\%}Fe_2O_3$@rGO and $Ni_{6\%}Fe_2O_3$@rGO, which are the most promising materials in terms of expected electrocatalytic activity based on the morphological and structural features previously discussed. In the XPS profile of Ni doped sample, peaks corresponding to Fe 2p, O 1 s, C 1 s, N 1 s, and Ni 2p are evident, whereas Mg doped sample exhibits peaks corresponding to Fe 2p, O 1 s, C 1 s, N 1 s, and Mg 2p (Fig. 5**a**). The sensitivity of XPS toward Mg is half that of Fe, and XPS

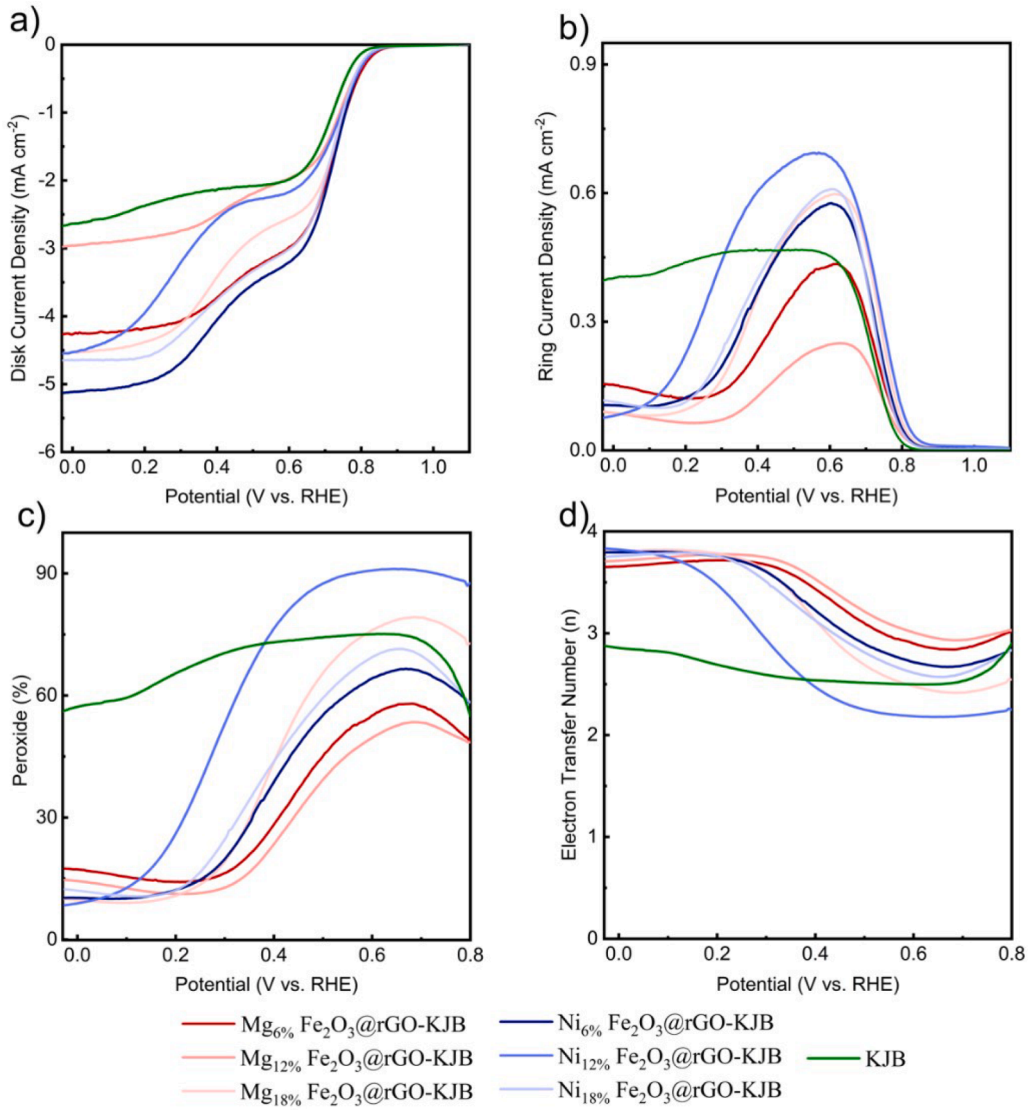

Fig. 6. Comparison of Mg and Ni doped Fe_2O_3@rGO with KJB and pure KJB, (a) Disk Current Densities, (b) Ring Current Densities, (c) Peroxide Production, (d) Electron Transfer Number.

is prone to carbon contamination. This, coupled with the XPS surface sensitivity and with the core-shell morphology of Mg doped sample, hindered Mg detection. On the contrary, Ni was well detected in Ni doped sample (Fig. 5**b**). The Ni 2p spectrum in Fig. 5**b** displays the $2p_{3/2}$ main peak at ~855 eV and a satellite at ~862 eV, revealing that the Ni atoms exist mostly in the 3+ oxidation state, suggesting that they may have been bonded to iron atoms. Another small peak at ~857 eV reveals the presence of the Ni^{2+} oxidation state. The appearance of the satellite peak suggests strong electronic interactions between nickel and iron oxides within the composite material. Such interactions play a vital role in improving both the catalytic properties and overall stability [36]. C1 s peaks depicted in Fig. 5**c,d** can be ascribed to sp^2-bonded carbon (C–C/C=C), epoxy and alkoxy groups (C–O), and carbonyl and carboxylic (O–C=O) groups, aligning with peaks observed at 284.8 eV, 286.2 eV, and 287.6 eV, respectively [37]. The peak positions of the three segments delineated in the O 1 s XPS spectrum (Fig. 5**e,f**) are 530.2 eV (Fe–O), 531.8 eV (C–O–Fe), and 533.4 eV (C–OH/C–O–C), confirming the linkage of Fe_2O_3 with graphene via the C–O–Fe bond in both $Ni_{6\%}$ modified and $Mg_{6\%}$ modified composites [38]. Fig. S5 presents the XPS spectra of both catalysts in the O 1 s region, revealing the presence of a peak corresponding to lattice oxygen as well as a higher-energy peak at 531.7 eV, which is associated with surface oxygen vacancies [36,39].

In the Fe 2p spectrum (Fig. 5**g,h**), two distinct peaks at ~710 eV and ~725 eV are observed for both catalysts, matching earlier reports of a spin–orbit doublet in Fe $2p_{3/2}$ and Fe $2p_{1/2}$. A peak at ~710.1 eV and ~725 eV indicates bivalent iron (Fe^{2+}), while a peak at ~713 eV reveals trivalent iron (Fe^{3+}) [40,36]. XPS analysis indicates that both materials are largely pure. These findings suggest the potential to introduce oxygen deficiencies as a component of the designed catalysts.

3.2. *Electrochemical measurements*

To evaluate the electrocatalytic activity, RRDE measurements have been carried out. The ORR performance has been analyzed using LSV in the oxygen-saturated alkaline electrolyte (0.1 M KOH). To analyze the electrocatalytic performance, the electrocatalysts were grinded-mixed with Ketjenblack (KJB). Fig. 6 shows the ORR activities of all the electrocatalysts-KJB composite at 1600 rpm.

Most of the electrocatalysts exhibit similar characteristics. In Fig. 6**a**, the disk current densities reveal a general trend where the system does not reach a total diffusion-limited regime. In addition, both the onset potential and half-wave potential are comparable across various samples, with the onset potential falling between 0.84 V (vs. RHE) for $Mg_{6\%}$-, $Mg_{12\%}$-, $Ni_{18\%}Fe_2O_3$@rGO and 0.83 V (vs. RHE) for the other samples

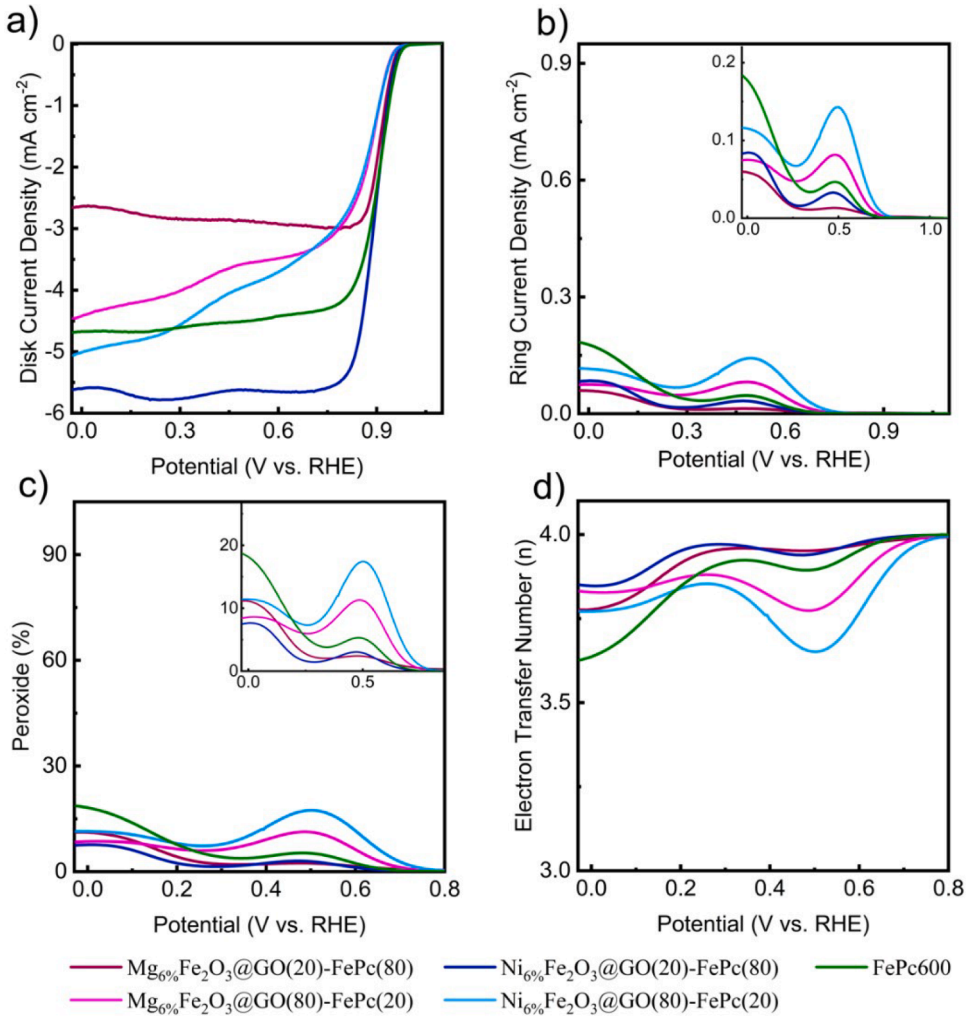

Fig. 7. Comparison between 2 composite $Mg_{6\%}$- and $Ni_{6\%}Fe_2O_3$@rGO/FePc600 80:20 and 20:80, (a) Disk Current Densities, (b) Ring Current Densities, (c) Peroxide Production and (d) Electron Transfer Number.

respectively. Notably, $Ni_{18\%}$-, $Ni_{6\%}$-, and $Mg_{6\%}Fe_2O_3$@rGO display the lowest half-wave potentials among the tested samples 0.72 V (vs. RHE) and 0.73 V (vs RHE), respectively. Furthermore, Fig. 6**b** shows a decrease in ring current densities compared to pure KJB, indicating a promising potential for these materials as peroxide scavengers. To quantify the peroxide anion, and thus the electrochemical selectivity of these materials, the following equation (Eq. (9)) has been used [41,42]:

$$\%Peroxide = \frac{2 * \frac{I_{ring}}{N}}{I_{disk} + \frac{I_{ring}}{N}} \quad (9)$$

Where I_{ring} and I_{disk} represent the current density values recorded a ring and disk electrodes, respectively, and N is the collection efficiency constant (0.37). Fig. 6**c** presents the percentage of peroxide production versus applied potential across all samples. In alignment with findings from Fig. 6**a** and **b**, the $Mg_{6\%}$ and $Ni_{6\%}$ samples show the lowest peroxide production relative to the achieved disk current density, reaching peak values of 57.9 % and 66.5 %, respectively. This reduced peroxide generation suggests an enhanced stability and effectiveness for these electrocatalysts in limiting undesirable by-products in the reaction process. The electron transfer number values have been calculated from disk and ring currents following Eq. 10 [41,42]

$$n = \frac{4 * I_{disk}}{I_{disk} + \frac{I_{ring}}{N}} \quad (10)$$

Fig. 6**d** shows the electron transfer number as a function of voltage. $Mg_{6\%}$- and $Ni_{6\%}Fe_2O_3$@rGO exhibit, across the voltage range analyzed, the higher electron transfer number, demonstrating an overall higher performance and thus a higher electrochemical selectivity compared to pure KJB. It is important to point out that among all the electrocatalyst $Mg_{12\%}Fe_2O_3$@rGO showed the lowest ring density and peroxide production with the highest electron number transfer. However, these electrocatalysts were not selected to proceed in the test due to their lowest disk current densities.

Based on prior data with pure KJB, the two most promising electrocatalysts, $Mg_{6\%}$- and $Ni_{6\%}Fe_2O_3$@rGO, were selected for testing as potential peroxide scavengers. To assess their peroxide scavenging abilities, these electrocatalysts were combined with a well-established ORR electrocatalyst, FePc600, in two different ratios: 80:20 and 20:80 FePc600 to $Mg_{6\%}$- or $Ni_{6\%}Fe_2O_3$@rGO, respectively. This setup aimed to analyze how varying compositions influence the overall peroxide mitigation effectiveness and provide insights into optimal electrocatalyst blending for enhanced performance.

Fig. 7 presents data for two composite material configurations, showing contrasting behaviors based on the electrocatalyst-to-FePc600 ratio. In the 80:20 composites, no significant improvements are

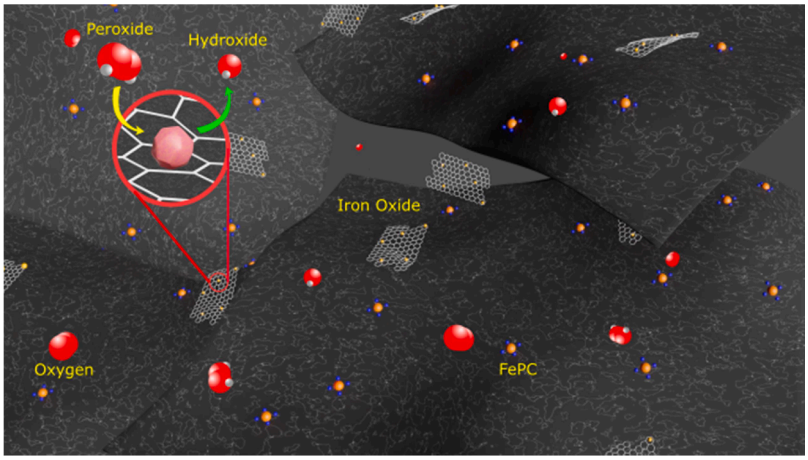

Fig. 8. Illustration depicting the peroxide scavenging properties of catalysts dispersed within the FePc600 matrix.

observed; the diffusion regime is not reached (Fig. 7**a**), and performance remains lower than pristine FePc600 in terms of ring current and peroxide production (Figs. 7**b-d**). However, the 20:80 composites reach a full diffusion regime with an overall 2.6 mA cm^{-2} and 5.6 mA cm^{-2} for $Mg_{6\%}$- and $Ni_{6\%}Fe_2O_3$@rGO (Fig. 7**a**). Notably, Fig. 7**b** reveals decreased ring current densities, indicating reduced peroxide production. Specifically, peroxide production for $Mg_{6\%}Fe_2O_3$@rGO and $Ni_{6\%}Fe_2O_3$@rGO composites at the 20:80 ratio is 2.4 % and 2.9 % (0.5 V vs. RHE), respectively, compared to 5.1 % for pure FePc600 (Fig. 7**d**). Additionally, both 80:20 composites show increased electron transfer number relative to pure FePc600, suggesting improved electrocatalytic efficiency. The $Ni_{6\%}Fe_2O_3$@rGO/FePc600 20:80 composite demonstrates remarkable performance, particularly with high disk current density and decreased peroxide production among the tested configurations. These qualities indicate its potential viability for industrial applications, where minimizing peroxide formation and maximizing current density are critical for high-performing low-cost materials (Fig. 8).

Tafel plots, corrected for mass transfer, were constructed for FePc600, $Ni_{6\%}Fe_2O_3$@rGO(20) FePc(80), and $Mg_{6\%}Fe_2O_3$@rGO(20) FePc(80) (Fig. S6). At higher positive potentials, the plots display linear behavior, while at more negative potentials, they become slightly curved [43]. The slopes of the linear regions were measured as −55.8, −51.3, and −55.2 mV per decade for the FePc600, $Ni_{6\%}Fe_2O_3$@rGO(20) FePc(80), and $Mg_{6\%}Fe_2O_3$@rGO(20)FePc(80) samples, respectively. The outstanding ORR activity of Ni-doped sample is further supported by its Tafel slope of −51 mV dec^{-1} within the low overpotential region. This value is lower than that of commercial Pt/C catalysts (−60 mV dec^{-1}) and the pure sample (−55 mV dec^{-1}), indicating enhanced catalytic performance [43,44].

4. Conclusions

In this study, we devised and explored an effective strategy aimed at improving the electrocatalytic performance and selectivity of the Fe_2O_3@rGO system. This was achieved through the incorporation of Mg and Ni modifiers, utilizing a cost-effective synthetic methodology. The electrochemical selectivity of both Fe_2O_3@rGO and its doped variants was rigorously assessed via RRDE analysis, revealing an overall enhancement across all doped electrocatalysts in comparison to the pristine one.

Remarkably, among the various catalysts studied, $Ni_{6\%}Fe_2O_3$@rGO doping demonstrated superior peroxide scavenging properties. This reduction in hydrogen peroxide production is significant for FC systems, as hydrogen peroxide is a harmful species for membranes and ORR performance [45,46]. The improved performance of these electrocatalysts was elucidated by the contraction in the primary unit cell observed by XRD, which, together with partial reduction of GO and formation of Oxygen vacancies, contribute to facilitating bulk electron conduction. In addition, the reduction of grain size, revealed by electron microscopy, facilitates grain-boundary electron exchange and interfacial charge transfer with the electroactive species.

Summarizing, this work contributes valuable insights to the relatively less-explored domain of iron oxide electrocatalysts. The study serves as a foundational exploration into enhancing oxide materials by modulating the band gap and inserting defects through doping, ultimately leading to improved peroxide scavenging for the potential use as cocatalyst material to decrease the inefficiency of electrocatalytic conversion in ORR reactions.

CRediT authorship contribution statement

Leonardo Balducci: Writing – original draft, Visualization, Methodology, Investigation, Formal analysis. **Mohsin Muhyuddin:** Investigation, Formal analysis. **Hamideh Darjazi:** Writing – review & editing, Visualization, Methodology, Investigation. **Giuseppina Meligrana:** Methodology, Investigation. **Carlo Santoro:** Writing – review & editing, Validation, Formal analysis. **Francesco Nobili:** Writing – review & editing, Validation, Supervision, Funding acquisition, Formal analysis.

Declaration of competing interest

The authors declare that they have no known competing financial interests or personal relationships that could have appeared to influence the work reported in this paper.

Supplementary materials

Supplementary material associated with this article can be found, in the online version, at doi:10.1016/j.electacta.2025.146088.

Data availability

Data will be made available on request.

References

[1] N. Sazali, W.N.W. Salleh, A.S. Jamaludin, M.N.M. Razali, New perspectives on fuel cell technology: a brief review, Membranes. (Basel) 10 (5) (2020), https://doi.org/10.3390/membranes10050099.
[2] X. Ren, Q. Lv, L. Liu, et al., Current progress of Pt and Pt-based electrocatalysts used for fuel cells, Sustain. Energy Fuels. 4 (1) (2019) 15–30, https://doi.org/10.1039/c9se00460b.

[3] M.D. Bhatt, J.Y. Lee, Advancement of platinum (Pt)-free (Non-Pt Precious Metals) and/or metal-free (Non-Precious-Metals) electrocatalysts in energy applications: a review and perspectives, Energy uels 34 (6) (2020) 6634–6695, https://doi.org/10.1021/acs.energyfuels.0c00953.

[4] Y. Nie, L. Li, Z. Wei, Recent advancements in Pt and Pt-free catalysts for oxygen reduction reaction, Chem. Soc. Rev. 44 (8) (2015) 2168–2201, https://doi.org/10.1039/c4cs00484a.

[5] M.A. Abbas, J.H. Bang, Rising again: opportunities and challenges for platinum-free electrocatalysts, Chem. Mater. 27 (21) (2015) 7218–7235, https://doi.org/10.1021/acs.chemmater.5b03331.

[6] J. Zhao, C. Fu, K. Ye, et al., Manipulating the oxygen reduction reaction pathway on Pt-coordinated motifs, Nat. Commun. 13 (1) (2022), https://doi.org/10.1038/s41467-022-28346-0.

[7] X. Ge, A. Sumboja, D. Wuu, et al., Oxygen reduction in alkaline Media: from mechanisms to recent advances of catalysts, ACS. Catal. 5 (8) (2015) 4643–4667, https://doi.org/10.1021/acscatal.5b00524.

[8] C. Santoro, A. Serov, C.W.N. Villarrubia, et al., High catalytic activity and pollutants resistivity using Fe-AAPyr cathode catalyst for microbial fuel cell application, Sci. Rep. 5 (2015), https://doi.org/10.1038/srep16596.

[9] K. Artyushkova, S. Rojas-Carbonell, C. Santoro, et al., Correlations between synthesis and performance of Fe-based PGM-free catalysts in acidic and alkaline Media: evolution of surface chemistry and morphology, ACS. Appl. Energy Mater. 2 (8) (2019) 5406–5418, https://doi.org/10.1021/acsaem.9b00331.

[10] S. Rojas-Carbonell, C. Santoro, A. Serov, P. Atanassov, Transition metal-nitrogen-carbon catalysts for oxygen reduction reaction in neutral electrolyte, Electrochem. commun. 75 (2017) 38–42, https://doi.org/10.1016/j.elecom.2016.12.011.

[11] S. Rojas-Carbonell, K. Artyushkova, A. Serov, C. Santoro, I. Matanovic, P. Atanassov, Effect of pH on the activity of platinum group metal-free catalysts in oxygen reduction reaction, ACS. Catal. 8 (4) (2018) 3041–3053, https://doi.org/10.1021/acscatal.7b03991.

[12] R. Gan, Y. Wang, W. Ma, et al., Fe2O3-encapsulated and Fe-nx-containing hierarchical porous carbon spheres as efficient electrocatalyst for oxygen reduction reaction, Int. J. Hydrogen. Energy 47 (4) (2022) 2103–2113, https://doi.org/10.1016/j.ijhydene.2021.10.157.

[13] T. Molodtsova, M. Gorshenkov, S. Kubrin, A. Saraev, A. Ulyankina, N. Smirnova, One-step access to bifunctional γ-Fe2O3/δ-FeOOH electrocatalyst for oxygen reduction reaction and acetaminophen sensing, J. Taiwan. Inst. Chem. Eng. (2022) 140, https://doi.org/10.1016/j.jtice.2022.104569.

[14] Q.Q. Xu, W. Huo, S.S. Li, et al., Crystal phase determined Fe active sites on Fe2O3 (γ- and α-Fe2O3) yolk-shell microspheres and their phase dependent electrocatalytic oxygen evolution reaction, Appl. Surf. Sci. (2020) 533, https://doi.org/10.1016/j.apsusc.2020.147368.

[15] X. Liu, W. Hu, Iron oxide/oxyhydroxide decorated graphene oxides for oxygen reduction reaction catalysis: a comparison study, RSC. Adv. 6 (35) (2016) 29848–29854, https://doi.org/10.1039/C5RA28038A.

[16] Z. Yao, Y. Li, D. Chen, et al., γ-Fe2O3 clusters embedded in 1D porous N-doped carbon matrix as pH-universal electrocatalyst for enhanced oxygen reduction reaction, Chem. Eng. J. (2021) 415, https://doi.org/10.1016/j.cej.2021.129033.

[17] X. Guo, S. Liu, X. Wan, et al., Controllable solid-phase fabrication of an Fe2O3/Fe5C2/Fe-N-C electrocatalyst toward optimizing the oxygen reduction reaction in zinc-air batteries, Nano Lett. 22 (12) (2022) 4879–4887, https://doi.org/10.1021/acs.nanolett.2c01318.

[18] M. Sun, G. Zhang, H. Liu, Y. Liu, J. Li, α- and γ-Fe2O3 nanoparticle/nitrogen doped carbon nanotube catalysts for high-performance oxygen reduction reaction, Sci. China Mater. 58 (9) (2015) 683–692, https://doi.org/10.1007/s40843-015-0082-x.

[19] S. Ren, S. Ma, Y. Yang, Q. Mao, C. Hao, Hydrothermal synthesis of Fe2O3/polypyrrole/graphene oxide composites as highly efficient electrocatalysts for oxygen reduction reaction in alkaline electrolyte, Electrochim. Acta 178 (2015) 179–189, https://doi.org/10.1016/j.electacta.2015.07.181.

[20] M. Muhyuddin, E. Berretti, S.A. Mirshokraee, et al., Formation of the active site structures during pyrolysis transformation of Fe-phthalocyanine into Fe-nx-C electrocatalysts for the oxygen reduction reaction, Appl. Catal. B 343 (2024), https://doi.org/10.1016/j.apcatb.2023.123515.

[21] M. Farahmandjou, F. Soflaee, Synthesis and characterization of α-Fe2O3 nanoparticles by simple co-precipitation method, Phys. Chem. Res. 3 (3) (2015) 191–196, https://doi.org/10.22036/pcr.2015.9193.

[22] A. Lassoued, B. Dkhil, A. Gadri, S. Ammar, Control of the shape and size of iron oxide (α-Fe2O3) nanoparticles synthesized through the chemical precipitation method, Results. Phys. 7 (2017) 3007–3015, https://doi.org/10.1016/j.rinp.2017.07.066.

[23] G. Yasin, M. Arif, M. Shakeel, et al., Exploring the nickel–Graphene nanocomposite coatings for superior corrosion resistance: manipulating the effect of deposition current density on its morphology, mechanical properties, and erosion-corrosion performance, Adv. Eng. Mater. 20 (7) (2018), https://doi.org/10.1002/adem.201701166.

[24] S. Bhattacharjee, A. Banerjee, K.K. Chattopadhyay, Field-enhanced polarization in polytype ferric oxides: confronting anisotropy in dielectric ellipsoid dispersion, J. Phys. D.: Appl. Phys. 54 (29) (2021), https://doi.org/10.1088/1361-6463/abf806.

[25] W. He, X. Li, S. An, T. Li, Y. Zhang, J. Cui, 3D β-Ni(OH)2 nanowires/RGO composite prepared by phase transformation method for superior electrochemical performance, Sci. Rep. 9 (1) (2019), https://doi.org/10.1038/s41598-019-47120-9.

[26] L. Balducci, H. Darjazi, E. Gonzalo, R. Cid, F. Bonilla, F. Nobili, Evaluation of electronic-ionic transport properties of a Mg/Zr-modified LiNi0.5Mn1.5O4 cathode for Li-ion batteries, ACS. Appl. Mater. Interfaces. 15 (48) (2023) 55620–55632, https://doi.org/10.1021/acsami.3c10480.

[27] S. Yang, Z. Qi, Y. Wen, et al., Generation of abundant oxygen vacancies in Fe doped δ-MnO2 by a facile interfacial synthesis strategy for highly efficient catalysis of VOCs oxidation, Chem. Eng. J. 452 (2023), https://doi.org/10.1016/j.cej.2022.139657.

[28] P. Katikaneani, A.K. Vaddepally, N. Reddy Tippana, R. Banavath, S. Kommu, Phase transformation of iron oxide nanoparticles from hematite to maghemite in presence of polyethylene glycol: application as corrosion resistant nanoparticle paints, J. Nanosci. 2016 (2016) 1–6, https://doi.org/10.1155/2016/1328463.

[29] S. Abe, M. Watanabe, Mg-induced phase transformation from hematite to maghemite, Mater. Res. Express. 1 (2) (2014), https://doi.org/10.1088/2053-1591/1/2/026108.

[30] B. Malik, S. Majumder, R. Lorenzi, et al., Promising electrocatalytic water and methanol oxidation reaction activity by nickel doped hematite/surface oxidized carbon nanotubes composite structures, Chempluschem. 87 (5) (2022), https://doi.org/10.1002/cplu.202200036.

[31] D.E. Fouad, C. Zhang, T.D. Mekuria, C. Bi, A.A. Zaidi, A.H. Shah, Effects of sono-assisted modified precipitation on the crystallinity, size, morphology, and catalytic applications of hematite (α-Fe2O3) nanoparticles: a comparative study, Ultrason. Sonochem. (2019) 59, https://doi.org/10.1016/j.ultsonch.2019.104713.

[32] H. Lee, Y.K. Park, S.J. Kim, et al., Facile synthesis of iron oxide/graphene nanocomposites using liquid phase plasma method, J. Nanosci. Nanotechnol. 16 (5) (2016) 4483–4486, https://doi.org/10.1166/jnn.2016.10995.

[33] J.M.J. Santillµn, D. Muçetónarboleda, D.C. Oral, et al., Optical and magnetic properties of Fe nanoparticles fabricated by femtosecond laser ablation in organic and inorganic solvents, Chemphyschem. 18 (9) (2017) 1192–1209, https://doi.org/10.1002/cphc.201601279.

[34] S. Biswal, D.S. Bhaskaram, G. Govindaraj, α-Fe2O3/reduced graphene oxide nanocomposite: interfacial effect on the magnetic property, J. Supercond. Nov. Magn. 33 (6) (2020) 1629–1632, https://doi.org/10.1007/s10948-019-05211-8.

[35] H. Hong, N.K. Memon, Z. Dong, B.H. Kear, S.D. Tse, Flame synthesis of gamma-iron-oxide (γ-Fe2O3) nanocrystal films and carbon nanotubes on stainless-steel substrates, Proc. Combust. Inst. 37 (1) (2019) 1249–1256, https://doi.org/10.1016/j.proci.2018.06.098.

[36] M.N. Shaddad, A.I. Alharthi, S.A. Aladeemy, P. Arunachalam, Engineering oxygen vacancy on nickel-doped iron oxide nanorods as efficient bifunctional electrocatalysts for oxygen evolution and urea oxidation reaction, J. Taiwan. Inst. Chem. Eng. (2025), https://doi.org/10.1016/j.jtice.2024.105928. Published online.

[37] T. Han, Y. Wei, X. Jin, et al., Hydrothermal self-assembly of α-Fe 2 O 3 nanorings@graphene aerogel composites for enhanced Li storage performance, J. Mater. Sci. 54 (9) (2019) 7119–7130, https://doi.org/10.1007/s10853-019-03371-5.

[38] G.D. Park, J.S. Cho, J.K. Lee, Y.C. Kang, Na-ion storage performances of FeSex and Fe2O3 hollow nanoparticles-decorated reduced graphene oxide balls prepared by nanoscale Kirkendall Diffusion process, Sci. Rep. 6 (2016), https://doi.org/10.1038/srep22432.

[39] R. Tian, Z. Gao, R. Lang, et al., Ru-functionalized Ni-doped dual phases of α/γ-Fe2O3 nanosheets for an optimized acetone detection, J. Nanostruct. Chem. 13 (6) (2023) 577–589, https://doi.org/10.1007/s40097-022-00475-4.

[40] R. Liu, Y. Xu, B. Chen, Self-assembled nano-FeO(OH)/reduced graphene oxide aerogel as a reusable catalyst for photo-fenton degradation of phenolic organics, Environ. Sci. Technol. 52 (12) (2018) 7043–7053, https://doi.org/10.1021/acs.est.8b01043.

[41] C. Santoro, A. Serov, R. Gokhale, et al., A family of Fe-N-C oxygen reduction electrocatalysts for microbial fuel cell (MFC) application: relationships between surface chemistry and performances, Appl. Catal. B 205 (2017) 24–33, https://doi.org/10.1016/j.apcatb.2016.12.013.

[42] C. Santoro, R. Gokhale, B. Mecheri, et al., Design of iron(II) phthalocyanine-derived oxygen reduction electrocatalysts for high-power-density microbial fuel cells, ChemSusChem. 10 (16) (2017) 3243–3251, https://doi.org/10.1002/cssc.201700851.

[43] S. Gupta, L. Qiao, S. Zhao, et al., Highly active and stable graphene tubes decorated with FeCoNi alloy nanoparticles via a template-free graphitization for bifunctional oxygen reduction and evolution, Adv. Energy Mater. 6 (22) (2016), https://doi.org/10.1002/aenm.201601198.

[44] A. Muthukrishnan, Y. Nabae, C.W. Chang, T. Okajima, T. Ohsaka, A high-performance Fe and nitrogen doped catalyst derived from diazoniapentaphene salt and phenolic resin mixture for oxygen reduction reaction, Catal. Sci. Technol. 5 (3) (2015) 1764–1774, https://doi.org/10.1039/c4cy01429d.

[45] Y. Li, M.Y. Chen, B.A. Lu, H.R. Wu, J.N. Zhang, Unravelling the role of hydrogen peroxide in pH-dependent ORR performance of Mn-N-C catalysts, Appl. Catal. B 342 (2024), https://doi.org/10.1016/j.apcatb.2023.123458.

[46] S. Rojas-Carbonell, K. Artyushkova, A. Serov, C. Santoro, I. Matanovic, P. Atanassov, Effect of pH on the activity of platinum group metal-free catalysts in oxygen reduction reaction, ACS. Catal. 8 (4) (2018) 3041–3053, https://doi.org/10.1021/acscatal.7b03991.